MULTIPHYSICS COMPUTATIONAL MODELING OF PHOTOMECHANICAL EFFECTS DURING INFRARED NEURAL STIMULATION

By

Mayna Hatram Nguyen

Thesis

Submitted to the Faculty of the

Graduate School of Vanderbilt University

in partial fulfillment of the requirements

for the degree of

MASTER OF SCIENCE

in

Biomedical Engineering

December 17, 2022

Nashville, Tennessee

Approved:

E. Duco Jansen, Ph.D.

Anita Mahadevan-Jansen, Ph.D.

ACKNOWLEDGEMENTS

I would like to acknowledge the Air Force Office of Scientific Research, which supported me through my NDSEG fellowship, the Repperger Internship program, and the equipment and supplies needed for the completion of this work by the AFOSR FA 9550-17-1-0374 grant.

I would like to thank my mentor at the Air Force Research Laboratory at San Antonio, TX, Mr. Chad Oian who helped make this work possible. I'd also like to thank Dr. William Roach for being my NDSEG mentor and offering support and advice during my time as a fellow.

I would like to thank my advisors, Dr. E. Duco Jansen and Dr. Anita Mahadevan-Jansen, who have been so supportive and guided me through this work. Thanks to their mentorship, I have learned so much about research and was encouraged to do my best work. I am so appreciative of them for believing in me, taking care of me during rough times, and letting me into their lives.

I would like to thank everyone at the Vanderbilt Biophotonics Center for being a part of my journey and a special thanks my current lab members: Parker Willmon, Jacob Hardenburger, Ezekiel Haugen, Han Dong, Trevor Voss, Sean Fitzgerald, and Alec Walter. Dr. Andrea Locke, you have given me so much helpful advice and I'm so thankful for that. I would especially like to acknowledge Anna Rourke, whose friendship I am so grateful for. Thank you for being the best supporter, I would not have been able to get through these past couple of years without you.

I am also so grateful to all the lab alum who have helped me and given me advice along the way: Dr. Graham Throckmorton, Dr. Jeremy Ford, Dr. Wilson Adams, Dr. Logan Jenkins, Dr. Laura Masson, and Dr. Mohit Ganguly.

Lastly, I'd like to thank my parents and brother for their unconditional love and support, and the friends outside of the lab who have supported me from afar. Without all of those listed and more, this work could not have completed, and I am so grateful for all you.

TABLE OF CONTENTS

LIST OF TABLES

LIST OF FIGURES

CHAPTER 1 Introduction

1.1 Optical Neural Modulation

It is estimated that more than 600 diseases affect the nervous system, with 9 million deaths and 276 million disabilities that occurred from neurological disorders worldwide in 2016[1]. Interfacing with the nervous system can be done with neuromodulation, which involves stimulating or blocking action potentials in the nervous system. Neuromodulation has three main applications: prosthetics to improve motor or cognitive neural function (including cochlear implants), therapy to treat neural diseases such as epilepsy, Parkinson's disease, depression, and traumatic brain injury, and neuroscience research to investigate the function of neurons and neural networks[2]. The current gold standard for neuromodulation is electrical stimulation, which is used clinically in deep brain stimulation, pacemakers, and other neuromodulation devices[3]. During electrical stimulation, electrodes are placed on the target neuron or nerve to apply a potential gradient[2]. However, this method of stimulation has limitations, such as the need for direct contact, the cause of a stimulation artifact, MRI incompatibility, and electrode complications[4–6]. In addition, spatial selectivity in electrical stimulation is also severely limited by current spread, which is an issue in the clinic as there is a need to target specific areas in the brain or fibers in the nervous system without affecting nearby areas. Consequently, there is a need for an alternate method of neuromodulation that overcomes these limitations.

Optogenetics has become a popular tool for optical neuromodulation since 2005, when Boyden *et al*. discovered that pulses of blue light elicited depolarizing spike trains in neurons expressing a microbial opsin gene, Channelrhodopsin-2. This discovery showed a promising way to precisely control neuronal activity with specific targeting of cells[7]. Opsins act as light-activated ion channels, allowing for quick and precise optical manipulation of biological processes[2]. Since 2005, several opsins have been discovered to be activated or inhibited by different wavelengths of light, with the three major classes of microbial proteins used for single-component optogenetics being bacteriorhodopsins, halorhodopsins (inhibitory), and channelrhodopsins[8]. However, one major drawback of optogenetics for human clinical use is that it requires genetic modification, which is challenging for clinical translation as it raises safety and ethical concerns.

Another emerging technique for neuromodulation is focused ultrasound. This non-invasive technique delivers mechanical forces to cells deep in tissue using pressure waves, which can be focused using interference of the incident waves. Despite ultrasound being able to evoke a response in both the central and peripheral nervous systems in several neuronal targets[9], the underlying mechanism is mostly unknown due to the multiple physical effects that occur. Recently it was shown that ultrasound produces a mechanical force, which results in extracellular calcium entering the cell through the activation of mechanosensitive channels. This calcium influx depolarizes the cell membrane and opens voltage-gated ion channels and stimulation. While a significant step towards understanding the mechanism has been made, more work is needed to further look at the precise forces caused by ultrasound and the specific roles of different mechanosensitive ion channels[10]. Moreover, there is also evidence that absorption or dissipation of the mechanical (kinetic) energy in ultrasound waves in tissue leads to local temperature increases and therefore a thermal component of ultrasound neuromodulation cannot be excluded[9,10].

1.2 Infrared Neural Stimulation

Another optical neuromodulation method, infrared neural stimulation (INS), emerged in 2005 when Wells *et al*. demonstrated the use of pulsed infrared light (λ=2.1-6.1 μm) to excite action potentials in *in vivo* rat sciatic nerves. A free-electron laser (FEL) was used for the initial studies, where it was shown that the radiant exposure threshold to evoke INS followed the water absorption curve, suggesting that the mechanism is likely to be primarily photothermal driven by water absorption. It was also shown that the optimal wavelengths for stimulation occurred at relative valleys in the water absorption curve, with ablation damage occurring at 2.5 times the stimulation threshold, suggesting that optical stimulation is a safe technique to modulate nerves[11,12]. INS was shown to be spatially selective (Figure 1.1), artifact-free, contact-free, and does not require genetic modification or exogenous compounds, and therefore overcomes many of the limitations of electrical stimulation[13]. Since its discovery, multiple studies have demonstrated the use of INS to modulate neural activity *in vitro* and in animal models such as *Aplysia* nerve, rat sciatic nerve, musk shrew vagus nerve, gerbil and cat auditory nerves, quail embryo hearts, non-human primate cortex, and even in dorsal roots in humans[13–18].

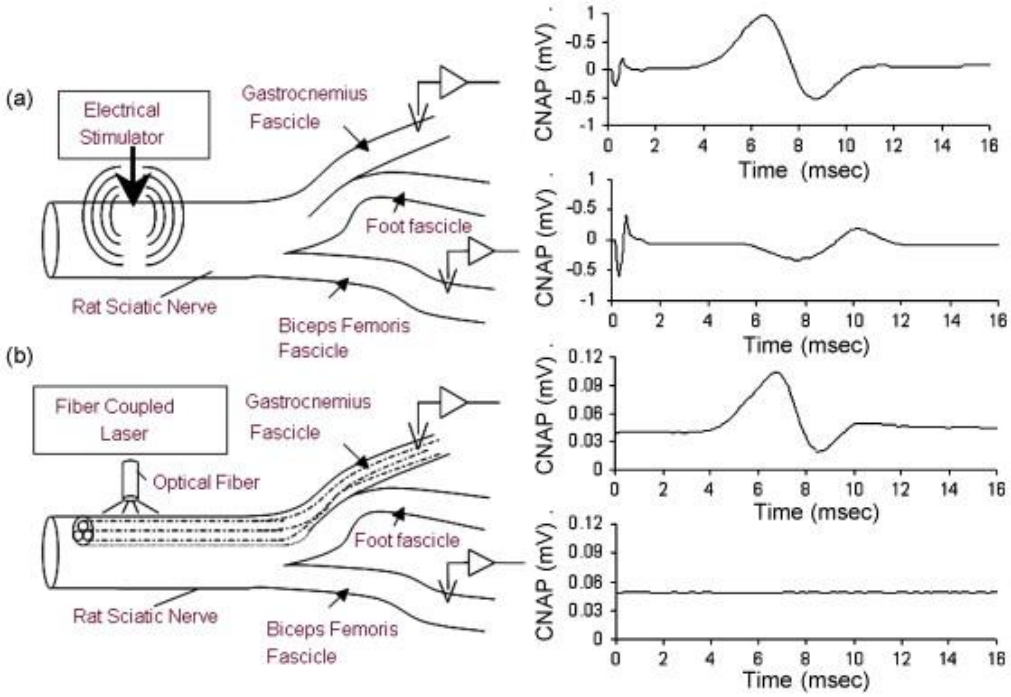

Figure 1.1 Infrared Neural Stimulation provides spatially selective targeting of nerves (a) Threshold compound muscle action potential (CMAP) response from electrical stimulation of the main branch of the rat sciatic nerve proximal to the first branch point (b) Corresponding results from threshold optical stimulation of specific target nerve fibers that innervates the gastrocnemius with no response from adjacent nerve fibers (quiet biceps femoris), showing selective optical stimulation. Figure from Wells *et al*. used with permission from Elsevier[13].

Wells *et al*. were also the first to look at the mechanism of INS. It was found that the laser energy is absorbed by chromophores in the tissue and is converted into a spatio-temporal thermal gradient which results in the excitation of the target cells[19]. Shapiro *et al*. investigated the mechanism of INS by recording currents of oocytes, human embryonic kidney cells, and lipid bilayers as they were stimulated with an infrared laser pulse. It was shown that the currents followed the temperature profiles, which consisted of a sharp rise followed by an exponential decay, confirming that INS does involve a temperature gradient. Furthermore, observing no change in current when adding or removing voltage-gated channels and blocking ion channels suggested that INS works on the most basic lipid bilayer, not just excitable cells. Experimental evidence of a transient change in membrane capacitance was also measured. The capacitance was further

investigated by developing a model based on the classical Gouy-Chapman-Stern theory of double-layer capacitors[20,21]. This model was later revised by Plaksin *et al*. to account for a modeling sign error[22] and thermally induced membrane deformations that were inferred from small-angle x-ray and neutron scattering measurements and molecular dynamics simulations. Overall, it was shown that there is a temperature-induced membrane capacitance increase of 0.3%/°C specifically due to the phospholipid bilayer membrane thinning axially and expanding laterally (Figure 1.2), which agrees with the experimental capacitance change that Shapiro *et al*. found. The observation of depolarization driven by a membrane capacitance change is a fundamental discovery toward understanding the INS mechanism. However, capacitance is unlikely to be the sole mechanism because the capacitance threshold needed to generate an action potential is higher than what Shapiro *et al*. and Plaksin *et al*. found[23].

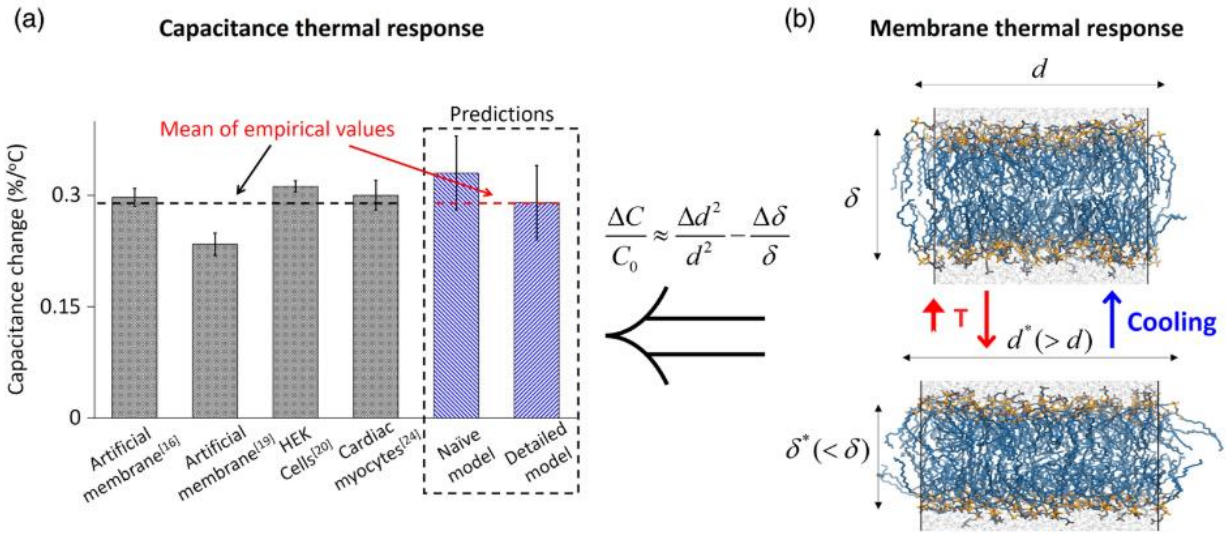

Figure 1.2 Capacitance increase due to changes in the bilayer lipid membrane. (a) Modeling and experimental results showing a 0.3%/°C increase in capacitance due to (b) the membrane decreasing in thickness and increasing in surface area from a temperature rise. Figure from Plaksin *et al*.[21] licensed under CC BY 4.0.

After Shapiro *et al*. looked at the membrane capacitance as a part of the mechanism, it was hypothesized that the thermal gradient destabilizes phospholipids in the membrane, causing

nanopores to form and allowing extracellular ions to flow in and depolarize the cell. Using fluorescent markers YO-PRO-1 and propidium, it was shown that impermeant cell ions were able to leak into the cell, suggesting that 1-2 nm transient pores were created. In addition, rapid transient increases in intracellular calcium were measured in primary hippocampal neurons, suggesting a depolarization due to nanopore formation. Nanopores are more likely to be formed when the lipid bilayer is in a phase transition, which is dependent on thermodynamic properties, including pressure and temperature. Thus, it is hypothesized that the membrane properties are altered by pressure, temperature, or a combination of the two[24].

Transient receptor potential vanilloid (TRPV) channels have been hypothesized to play a role in INS, but details remain unclear. A thermal gradient and not absolute temperature appears to drive stimulation[19], so TRPV channels would not be implicated since they activate at an absolute temperature threshold. However, some studies that used channel blockers have shown evidence that TRPV channels are involved. In a pharmacological study, TRPV4 channels were proven to play a role in laser-evoked responses in sensory neurons[25]. Other studies implicated TRPV1 as responsible for stimulation in both rat vagus nerves and mice auditory nerves[26,27]. While it appears that the INS mechanism has a photothermal component, more work is needed to determine what exactly drives INS, both biophysically and what the underlying neural effects are from the biophysics.

Laser-induced stress and volumetric thermal expansion have previously been considered as the mechanism, but the conclusions from the experimental results dismissed a photomechanical contribution to the mechanism[19]. Since then, supporting evidence of a mechanical component to the mechanism has been more apparent with different stimulation thresholds at shorter pulses[20,28,29] and a possible mechanical mechanism in cochlear stimulation[30–32]. Additionally, various mechanosensitive channels have been investigated for ultrasound stimulation. Yoo *et al*. found that in cortical neurons, mechanosensitive channels TRPP1/2, TRPC1, and Piezo1 respond to mechanical interactions, which then opens TRPM4 channels and causes depolarization[10]. TRAAK K^+ channels in Xenopus oocytes were found to be sensitive to pressure (-15mmHg = -2000Pa), which caused channel opening due to membrane tension [33]. Piezo2 was observed to be essential for mechanical firing in a subset of mouse sensory neurons[34]. Kubanek *et al*. showed that focused ultrasound modulates K^+ and Na^+

currents through K2P and $Na_v1.5$ channels[35]. Based on these findings, a mechanical component could potentially be involved in the INS mechanism.

1.3 Computational Modeling of Laser Tissue Interactions

1.3.1 Optical Interactions

As laser light irradiates tissue, specific interactions occur based on the tissue optical properties. At the surface, some light undergoes reflection while the remaining light refracts based on the angle of incidence and refraction index of the tissue. Some light gets absorbed, where it is converted into heat, and the remaining light scatters and propagates through the tissue. The radiative transport equation describes the transfer of energy through a medium and is written as:

$$\frac{dL(r,\hat{s})}{ds} = \mu_a L(r,\hat{s}) - \mu_s L(r,\hat{s}) + \int_0^{4\pi} p(\hat{s},\hat{s}')L(r,\hat{s})d\omega' + S(r,\hat{s})$$

where L [$W/m^2 \cdot sr$] is the radiance, μ_a [1/m] is the absorption coefficient, μ_s [1/m] is the scattering coefficient, p is the scattering phase function [1/sr], and S is the optical source generated at r in direction s [36]. However, the radiative transport equation cannot easily be solved in the closed form. Therefore, approximations and stochastic methods, such as Monte Carlo simulations, have been used to approximate the solution to modeling light transport in tissue.

Monte Carlo is a statistical method that uses random sampling of variables from probability distributions. Monte Carlo for light transport in biological tissue was first implemented in 1983 by Adams and Wilson[37]. Since then, Prahl *et al*. introduced the inclusion of boundary conditions and anisotropic scattering in 1989[38], and the first open-source multilayer Monte Carlo simulator MCML was developed by Wang and Jacques in 1995[39]. Recently, Monte Carlo has evolved to be GPU-accelerated and in-browser with the development of MCX Cloud[40,41]. The process of using Monte Carlo for light propagation starts by initializing photons with a weight of 1. The step size s is determined by randomly sampling the photon's free path based on the absorption and scattering coefficients, which add to form the total attenuation coefficient μ_t [1/m]. With ζ as a random number between 0 and 1, the step size is calculated as:

$$s = \frac{-\ln(\zeta)}{\mu_t}$$

The photon is then moved the step size s and a portion of the photon weight is deposited. The amount of deposited weight is stored in the corresponding position and is calculated by:

$$\Delta W = W\frac{\mu_a}{\mu_t}$$

If the photon's weight falls below some threshold value the photon is terminated. A roulette technique is used to determine if a photon should be terminated. This technique allows for energy conservation by only terminating photons with weight w a chosen fraction of the time (1 in m chance), and the remaining photon has an increased weight mw to allow it to continue to propagate. Otherwise, the photon is scattered based on the deflection angle θ and the azimuthal angle ψ. The deflection angle is based on the anisotropy g, which indicates forward scattering with a value close to 1 or backward scattering with a value close to -1, and the Henyey-Greenstein probability density function for scattering. The scattering angle is calculated as:

$$\cos(\theta) = \frac{1 + g^2 - (\frac{1 - g^2}{1 - g + 2g\zeta})^2}{2g}$$

Where ζ is a random number between 0 and 1. If there is isotropic scattering (g = 0), then the angle is calculated as:

$$\cos(\theta) = 2\zeta - 1$$

And the azimuthal angle is calculated as:

$$\psi = 2\pi\zeta$$

Where ζ is a random number uniformly distributed between 0 and 1. When a photon encounters a boundary, the photon is either reflected or transmitted. To handle a boundary, a fraction of the photon escapes as reflectance (if at the surface) or transmittance (if at the bottom), and the remaining photon weight is internally reflected into the tissue to continue propagating[36]. Ultimately, Monte Carlo simulations compute the spatial distribution of absorbed photons and thus the heat source S(r,z) for a 2D distribution or S(x,y,z) for a 3D distribution. A 2D distribution is useful for symmetric, radial problems, while 3D distributions are needed for asymmetric problems.

1.3.2 Photothermal interactions

When laser light is absorbed in tissue, this results in a thermal energy that is deposited in the tissue. The local temperature rise at a given point at the end of a short, thermally confined laser pulse with a pulse duration of Δt can be estimated as:

$$\Delta T(x,y,z) = \frac{\mu_a \phi(x,y,z)\Delta t}{\rho c}$$

where μ_a is the absorption coefficient [1/m], ϕ is the fluence rate [W/m^2], ρ is the density [kg/m^3], and c is the specific heat capacity [J/kg·K][36]. Heat transfer in tissue mainly occurs due to conduction, when heat is transferred due to a temperature gradient or driving force.

The Fourier heat equation is typically applied to calculate how temperature varies with space and time and is determined by the thermal conductivity κ [W/m·K]:

$$\rho c \frac{\partial T}{\partial t} = \nabla \cdot (\kappa \nabla T)$$

Computational modeling of heat transfer in tissue follows the traditional Pennes bioheat equation[36,42] since this takes into account the thermal interaction of tissues with blood perfusion:

$$\rho c \frac{\partial T}{\partial t} = \nabla \cdot (\kappa \nabla T) + \omega p_b c_b (T_b - T) + \dot{Q}_{met}$$

where ρ is density [kg/m^3], c is specific heat capacity [J/kg·K], κ is thermal conductivity [W/m·K], ω is the perfusion coefficient [1/s], and ρ_b, c_b, and T_b are the density, specific heat, and temperature, respectively of the perfusive medium. $\dot{Q}_{met}$ is the heat generated from metabolism. To account for the heat from the laser source $\dot{Q}_{source}$ [W/m^3], the equation is modified to:

$$\rho c \frac{\partial T}{\partial t} = \nabla \cdot (\kappa \nabla T) + \omega p_b c_b (T_b - T) + \dot{Q}_{met} + \dot{Q}_{source}$$

A convective boundary condition occurs at the surface of a tissue, which in our case, is a nerve exposed to air. Convection involves a heat exchange between a solid at a different temperature from flowing air or fluid. Newton's law of cooling describes this convective flow $\dot{Q}_s$ [W] as:

$$\dot{Q}_s = hA(T_\infty - T_s)$$

where h is the convective coefficient [$W/m^2 \cdot K$], A as the interface area, and the temperature of the surface T_s and bulk fluid T_∞ [K][36]. Solutions to determine the temperature distribution over time from laser irradiation typically involve modeling schemes such as finite-difference or finite-element modeling[43–45] and have been implemented for many years.

1.3.3 Photomechanical interactions

Photomechanical interactions are mostly known to occur through the explosive vaporization of tissue during ablation or the direct generation of pressure waves, but other mechanical effects such as surface displacement from volumetric expansion can also be observed. Pressure waves can be generated in three ways, thermoelastic expansion from the heating of tissue by a pulsed laser, material recoil caused by ablation, or the collapse of vapor cavitations. Due to our application of INS, which uses relatively low radiant exposures (well below the ablation threshold), this thesis will focus on generating pressure waves from thermoelastic expansion as well as surface displacement from volumetric expansion. Thermoelastic expansion typically requires stress confinement, which is when the duration of the laser pulse is shorter than the stress confinement time τ_{str}, which is the time it takes for the pressure to diffuse out of the irradiated volume and is calculated by:

$$\tau_{str} = \frac{\delta}{\sigma}$$

Where δ is the penetration depth of the tissue [m] and σ is the speed of sound in tissue (1500 m/s) [36].

In Figure 1.3, the confinement zones are shown for different pulse durations and penetration depths.

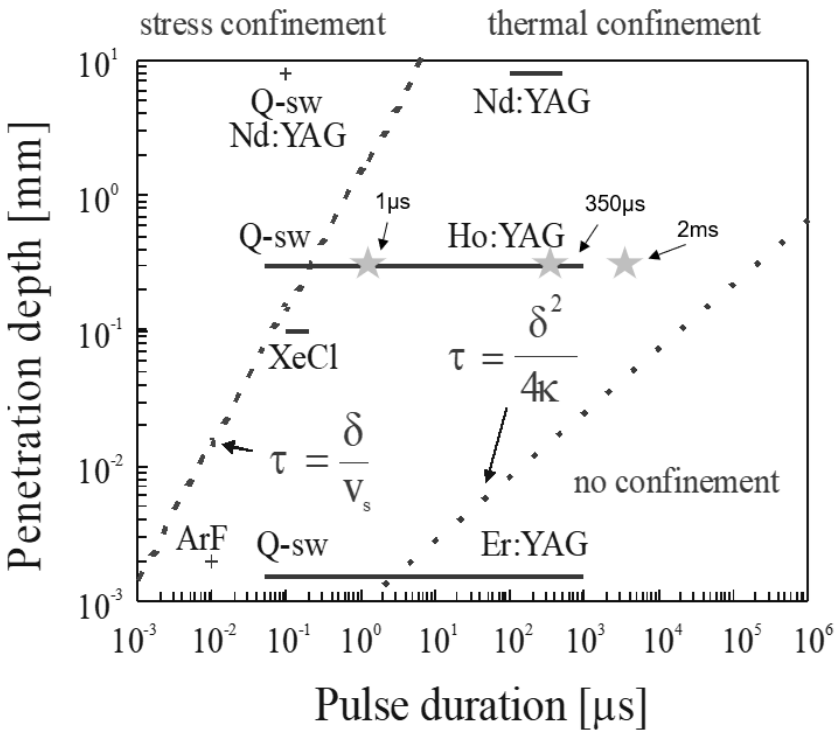

Figure 1.3 Stress and thermal confinement zones shown as a function of penetration depth and pulse duration. Stars indicate typical INS pulse durations and the corresponding penetration depth for λ = 1470nm and 2120nm. Adapted from Jacques 1993[46].

Typical INS parameters include using lasers in the IR range that are near a water absorption peak, such as a Ho:YAG laser at 2120 nm. Previous pulse durations have included a 350 µs pulse and a 2 ms pulse from a 1470nm diode laser with a similar absorption coefficient. These pulses are clearly thermally confined. However, the Ho:YAG 350 µs pulse has a 1 µs spike at the beginning of the pulse[28], which is much closer to stress confinement, so mechanical effects such as pressure waves from thermoelastic expansion are possible, even if small. The pressure can be related to the thermal expansion by the Grüneisen parameter Γ, which is the conversion efficiency from thermal to mechanical energy. The equation describing the pressure increase ΔP is:

$$\Delta P(z) = \Gamma \mu_a H(z)$$

Where H(z) is the depth-dependent fluence distribution [J/m^2][36].

1.3.4 SESE Model

The Scalable Effects Simulation Environment (SESE) is a computer program developed for the Air Force Research Laboratory by Nanohmics (Austin, TX) that combines an optical, thermal, and mechanical model to simulate the physical effects of materials due to laser irradiation (Figure 1.4). Full details of SESE can be found in the publicly available technical report[47], but the model components are described briefly here.

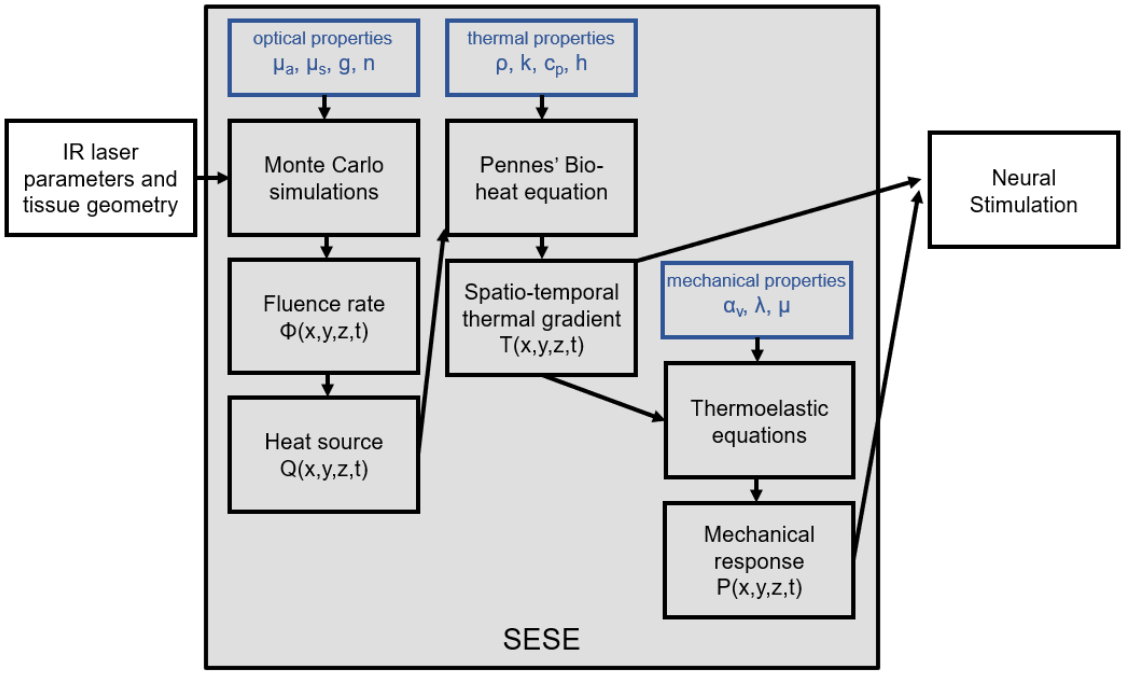

Figure 1.4 Overview of SESE Model showing the optical, thermal, and mechanical components, inputs, and outputs.

The optical component utilizes a Monte Carlo propagation technique with ray tracing to simulate absorption, scattering, reflection, and refraction. The temperature distribution is calculated using a finite-volume discretization and a red-black successive over-relaxation (RBSOR) method to solve the heat equation with the benefits of rapid convergence and parallelization[48]. SESE v.2.6.0 includes the addition of the capability to model photoacoustic effects. A finite-difference time-domain method is used to solve the linear-elastic wave equation, which couples to the photothermal solver with a source term that accounts for the thermal

expansion of the material. SESE also has the capability to determine thermal and chemical damage, but this is out of the scope of this thesis. SESE's photoacoustic approach is summarized as follows, with the variables defined in Table 1.1.

Starting with an equivalent of Newton's second law of motion, a momentum density is related to a force density generated by the stress tensor:

$$\rho \dot{\mathrm{v}} = \nabla \cdot \sigma + f$$

This is then integrated to get v, the displacement velocity, and again to obtain $\dot{u}$, the displacement:

$$\mathrm{v} = \dot{u}$$

From v, the strain rate $\dot{\varepsilon}$ is calculated:

$$\dot{\varepsilon} = S : (\nabla \mathrm{v})$$

Lastly, the stress tensor is calculated by integrating:

$$\dot{\sigma} = \lambda I\,(I : \dot{\varepsilon}) + 2\mu\dot{\varepsilon} - \alpha v\left(\lambda + \frac{2}{3}\mu\right)\dot{w}I$$

Parameter	**Symbol**	**Units**
Density	ρ	kg/m^3
Force density	f	N/m^3
Displacement velocity	v	m/s
Displacement	$\dot{u}$	m
Strain rate	$\dot{\varepsilon}$	--
Symmetrization operator	S	--
Stress tensor	σ	Pa
Elastic modulus	λ	Pa
Rank 2 identity tensor	I	--
Shear modulus	μ	Pa
Thermal expansion coefficient	α_v	1/K
Temperature rate	$\dot{w}$	--

Table 1.1 Summary of variables used in SESE mechanical model

For visualization of the simulation results, ParaView was used to analyze model outputs in 3D space over time and to extract data as needed. The work in this thesis focuses on using SESE as it provides a combined optical, thermal, and mechanical model for laser irradiation and allows for flexible geometries with various and tunable material properties.

Computational models provide valuable insights into the physical processes that are on the microscopic scale and are difficult to determine experimentally. Therefore, the model should be validated before employing SESE as a tool to ensure accurate results. For each of the optical, thermal, and mechanical components, SESE has been verified against analytical solutions and other models[47]. Additionally, SESE has been validated against experimental skin damage thresholds for the thermal model[49,50]. Since the photoacoustic model in SESE is a recent addition, experimental validation has yet to be published but is addressed in Chapter 2 of this thesis.

Based on the potential involvement of mechanosensitive ion channels, evidence of a photomechanical mechanism in cochlear stimulation, and the fact that shorter pulses are closer to stress confinement than longer pulses, we hypothesize that a mechanical component is involved in shorter pulses that results in more efficient stimulation. Using computational modeling, we can obtain an understanding of the underlying biophysics during an infrared pulse on an incident nerve. This thesis aims to use and validate an optical-thermal-mechanical computational model to investigate mechanical effects in peripheral nerve INS. The transient pressure waves and displacement modeling results will be compared to experimental stimulation thresholds at different pulse widths to gain insight into a potential mechanical component that is involved in the INS mechanism.

1.4 References

1. Dumurgier J, Tzourio C. Epidemiology of neurological diseases in older adults. *Rev Neurol (Paris)*. 2020;176(9):642-648. doi:10.1016/J.NEUROL.2020.01.356

2. Luan S, Williams I, Nikolic K, Constandinou TG. Neuromodulation: Present and emerging methods. *Front Neuroeng*. 2014;7(JUL):27. doi:10.3389/FNENG.2014.00027/BIBTEX

3. Gildenberg PL. Evolution of Neuromodulation. *Stereotact Funct Neurosurg*. 2005;83:71-79. doi:10.1159/000086865

4. Mandrile F, Farina D, Pozzo M, Merletti R. Stimulation Artifact in Surface EMG Signal: Effect of the Stimulation Waveform, Detection System, and Current Amplitude Using Hybrid Stimulation Technique. *IEEE Trans Neural Syst Rehabil Eng*. 2003;11(4):407-415. doi:10.1109/TNSRE.2003.819791

5. Ballestero J, Recugnat M, Laudanski J, et al. Reducing Current Spread by Use of a Novel Pulse Shape for Electrical Stimulation of the Auditory Nerve. *Trends Hear*. 2015;19. doi:10.1177/2331216515619763

6. Oh MY, Abosch A, Kim SH, Lang AE, Lozano AM. Long-term Hardware-related Complications of Deep Brain Stimulation. *Neurosurgery*. 2002;50(6):1268-1276. Accessed November 18, 2021. https://academic.oup.com/neurosurgery/article/50/6/1268/2739846

7. Boyden ES, Zhang F, Bamberg E, Nagel G, Deisseroth K. Millisecond-timescale, genetically targeted optical control of neural activity. *Nat Neurosci 2005 89*. 2005;8(9):1263-1268. doi:10.1038/nn1525

8. Deisseroth K. Optogenetics: 10 years of microbial opsins in neuroscience. *Nat Neurosci 2015 189*. 2015;18(9):1213-1225. doi:10.1038/nn.4091

9. Blackmore J, Shrivastava S, Sallet J, Butler CR, Cleveland RO. Ultrasound Neuromodulation: A Review of Results, Mechanisms and Safety. *Ultrasound Med Biol*. 2019;45(7):1509-1536. doi:10.1016/J.ULTRASMEDBIO.2018.12.015

10. Yoo S, Mittelstein DR, Hurt RC, Lacroix J, Shapiro MG. Focused ultrasound excites cortical neurons via mechanosensitive calcium accumulation and ion channel amplification. *Nat Commun 2022 131*. 2022;13(1):1-13. doi:10.1038/s41467-022-28040-1

11. Wells J, Kao C, Mariappan K, et al. Optical stimulation of neural tissue in vivo. *Opt Lett*. 2005;30(5):504. doi:10.1364/ol.30.000504

12. Wells J, Kao C, Jansen ED, Konrad P, Mahadevan-Jansen A. Application of infrared light for in vivo neural stimulation. *J Biomed Opt*. 2005;10(6):064003. doi:10.1117/1.2121772

13. Wells J, Konrad P, Kao C, Jansen ED, Mahadevan-Jansen A. Pulsed laser versus electrical energy for peripheral nerve stimulation. *J Neurosci Methods*. 2007;163(2):326-337. doi:10.1016/J.JNEUMETH.2007.03.016

14. Duke AR, Lu H, Jenkins MW, Chiel HJ, Jansen ED. Spatial and temporal variability in response to hybrid electro-optical stimulation. *J Neural Eng*. 2012;9(3):036003. doi:10.1088/1741-2560/9/3/036003

15. Izzo AD, Richter CP, Jansen ED, Walsh JT. Laser stimulation of the auditory nerve. *Lasers Surg Med*. 2006;38(8):745-753. doi:10.1002/LSM.20358

16. Jenkins MW, Duke AR, Gu S, et al. Optical pacing of the embryonic heart. *Nat Photonics 2010 49*. 2010;4(9):623-626. doi:10.1038/nphoton.2010.166

17. Cayce JM, Kao CC, Malphrus JD, Konrad PE, Mahadevan-Jansen A, Jansen ED. Infrared neural stimulation of thalamocortical brain slices. *IEEE J Sel Top Quantum Electron*. 2010;16(3):565-572. doi:10.1109/JSTQE.2009.2032424

18. Cayce JM, Wells JD, Malphrus JD, et al. Infrared neural stimulation of human spinal nerve roots in vivo. *https://doi.org/101117/1NPh21015007*. 2015;2(1):015007. doi:10.1117/1.NPH.2.1.015007

19. Wells J, Kao C, Konrad P, et al. Biophysical mechanisms of transient optical stimulation of peripheral nerve. *Biophys J*. 2007;93(7):2567-2580. doi:10.1529/biophysj.107.104786

20. Shapiro MG, Homma K, Villarreal S, Richter CP, Bezanilla F. Infrared light excites cells by changing their electrical capacitance. *Nat Commun*. 2012;3(1):1-11.

doi:10.1038/ncomms1742

21. Plaksin M, Shapira E, Kimmel E, Shoham S. Thermal Transients Excite Neurons through Universal Intramembrane Mechanoelectrical Effects. *Phys Rev X*. 2018;8(1):011043. doi:10.1103/PhysRevX.8.011043

22. Plaksin M, Kimmel E, Shoham S. Correspondence: Revisiting the theoretical cell membrane thermal capacitance response. *Nat Commun 2017 81*. 2017;8(1):1-2. doi:10.1038/s41467-017-00435-5

23. Peterson EJ, Tyler DJ. Activation using infrared light in a mammalian axon model. *Proc Annu Int Conf IEEE Eng Med Biol Soc EMBS*. Published online 2012:1896-1899. doi:10.1109/EMBC.2012.6346323

24. Beier HT, Tolstykh GP, Musick JD, Thomas RJ, Ibey BL. Plasma membrane nanoporation as a possible mechanism behind infrared excitation of cells. *J Neural Eng*. 2014;11(6):066006. doi:10.1088/1741-2560/11/6/066006

25. Albert ES, Bec JM, Desmadryl G, et al. TRPV4 channels mediate the infrared laser-evoked response in sensory neurons. *J Neurophysiol*. 2012;107(12):3227-3234. doi:10.1152/JN.00424.2011/ASSET/IMAGES/LARGE/Z9K0111213780007.JPEG

26. Rhee A, Li G, Wells J, et al. Photostimulation of sensory neurons of the rat vagus nerve. In: *Https://Doi.Org/10.1117/12.772037*. Vol 6854. SPIE; 2008:69-73. doi:10.1117/12.772037

27. Suh E, Izzo Matic A, Otting M, et al. Optical stimulation in mice lacking the TRPV1 channel. In: *Https://Doi.Org/10.1117/12.816891*. Vol 7180. SPIE; 2009:112-116. doi:10.1117/12.816891

28. Throckmorton G, Cayce J, Ricks Z, Adams WR, Jansen ED, Mahadevan-Jansen A. Identifying optimal parameters for infrared neural stimulation in the peripheral nervous system. *Neurophotonics*. 2021;8(1):015012. doi:10.1117/1.NPH.8.1.015012

29. Farah N, Zoubi A, Matar S, et al. Holographically patterned activation using photo-absorber induced neural–thermal stimulation. *J Neural Eng*. 2013;10(5):056004. doi:10.1088/1741-2560/10/5/056004

30. Izzo AD, Walsh JT, Ralph H, et al. Laser Stimulation of Auditory Neurons: Effect of Shorter Pulse Duration and Penetration Depth. *Biophys J*. 2008;94(8):3159-3166. doi:10.1529/BIOPHYSJ.107.117150

31. Teudt IU, Maier H, Richter CP, Kral A. Acoustic events and "optophonic" cochlear responses induced by pulsed near-infrared LASER. *IEEE Trans Biomed Eng*. 2011;58(6):1648-1655. doi:10.1109/TBME.2011.2108297

32. Schultz M, Baumhoff P, Maier H, et al. Nanosecond laser pulse stimulation of the inner ear—a wavelength study. *Biomed Opt Express*. 2012;3(12):3332. doi:10.1364/BOE.3.003332

33. Sorum B, Rietmeijer RA, Gopakumar K, Adesnik H, Brohawn SG. Ultrasound activates mechanosensitive TRAAK K+ channels through the lipid membrane. *Proc Natl Acad Sci U S A*. 2021;118(6):e2006980118. doi:10.1073/PNAS.2006980118/SUPPL_FILE/PNAS.2006980118.SAPP.PDF

34. Hoffman BU, Baba Y, Lee SA, Tong CK, Konofagou EE, Lumpkin EA. Focused ultrasound excites action potentials in mammalian peripheral neurons in part through the mechanically gated ion channel PIEZO2. *Proc Natl Acad Sci U S A*. 2022;119(21):e2115821119. doi:10.1073/PNAS.2115821119/SUPPL_FILE/PNAS.2115821119.SAPP.PDF

35. Kubanek J, Shi J, Marsh J, Chen D, Deng C, Cui J. Ultrasound modulates ion channel currents. *Sci Reports 2016 61*. 2016;6(1):1-14. doi:10.1038/srep24170

36. Welch AJ, Van Gemert MJC. *Optical-Thermal Response of Laser-Irradiated Tissue*. Springer Netherlands; 2011. doi:10.1007/978-90-481-8831-4/COVER

37. Wilson BC, Adam G. *A Monte Carlo Model for the Absorption and Flux Distributions of Light in Tissue*. Vol 10.; 1983. doi:10.1118/1.595361

38. Prahl A Prahl SS, Monte Carlo A, Prahl S, Keijzer M, Jacques S, Welch A. A Monte Carlo model of light propagation in tissue. *https://doi.org/101117/122283590*. 1989;10305(10):105-114. doi:10.1117/12.2283590

39. Wang L, Jacques SL, Zheng L. MCML—Monte Carlo modeling of light transport in

multi-layered tissues. *Comput Methods Programs Biomed*. 1995;47(2):131-146. doi:10.1016/0169-2607(95)01640-F

40. Fang Q, Boas DA, Boas DA, et al. Monte Carlo Simulation of Photon Migration in 3D Turbid Media Accelerated by Graphics Processing Units. *Opt Express, Vol 17, Issue 22, pp 20178-20190*. 2009;17(22):20178-20190. doi:10.1364/OE.17.020178

41. Yan S, Fang Q. Hybrid mesh and voxel based Monte Carlo algorithm for accurate and efficient photon transport modeling in complex bio-tissues. *Biomed Opt Express*. 2020;11(11):6262. doi:10.1364/BOE.409468

42. PENNES HH. Analysis of Tissue and Arterial Blood Temperatures in the Resting Human Forearm. *https://doi.org/101152/jappl19481293*. 1948;1(2):93-122. doi:10.1152/JAPPL.1948.1.2.93

43. Choi B, Welch AJ. *Analysis of Thermal Relaxation During Laser Irradiation of Tissue*. Vol 29.; 2001.

44. Welch A. *The Thermal Response of Laser Irradiated Tissue*.; 1984. doi:10.1109/JQE.1984.1072339

45. Glenn TN, Rastegar S, Jacques SL. *Finite Element Analysis of Temperature Controlled Coagulation in Laser Irradiated Tissue*. Vol 43.; 1996.

46. Jacques SL. Role of tissue optics and pulse duration on tissue effects during high-power laser irradiation. *Appl Opt Vol 32, Issue 13, pp 2447-2454*. 1993;32(13):2447-2454. doi:10.1364/AO.32.002447

47. Zollars BG, Early EA, Thomas RJ, Elpers GJ, Goodwin AL, Gamez NJ. Scalable Effects Simulation Environment (SESE) Version 2.5.0. Published online July 12, 2019. Accessed October 25, 2021. https://apps.dtic.mil/sti/citations/AD1082675

48. Zhang C, Lan H, Ye Y, Estrade BD. *Parallel SOR Iterative Algorithms and Performance Evaluation on a Linux Cluster*.; 2005. Accessed September 13, 2022. https://apps.dtic.mil/sti/citations/ADA449212

49. Delisi MP, Schmidt MS, Hoffman AF, et al. Thermal damage thresholds for multiple-

pulse porcine skin laser exposures at 1070 nm. *https://doi.org/101117/1JBO253035001*. 2019;25(3):035001. doi:10.1117/1.JBO.25.3.035001

50. DeLisi MP, Gamez NJ, ClarkIII CD, Kumru SS, Rockwell BA, Thomas RJ. Computational modeling and damage threshold prediction of continuous-wave and multiple-pulse porcine skin laser exposures at 1070 nm. *J Laser Appl*. 2021;33(2):022023. doi:10.2351/7.0000367

CHAPTER 2 Multiphysics computational modeling of photomechanical effects during infrared neural stimulation

2.1 Introduction

Infrared Neural Stimulation (INS) is a technique that uses pulsed infrared light to excite action potentials in neural tissue. The initial INS studies utilized a free-electron laser (FEL) and suggested a photothermal mechanism where the laser energy is absorbed by chromophores in the tissue and is converted into thermal energy which results in the excitation of the target cells. Unlike traditional electrical stimulation, INS has unique characteristics such as being spatially selective, contact-free, and not having the large stimulation artifact that electrical stimulation has[1,2]. Since its discovery, multiple studies have demonstrated the use of INS to modulate neural activity *in vitro* and in animal models such as *Aplysia* nerve, rat sciatic nerve, musk shrew vagus nerve, gerbil and cat auditory nerves, quail embryo hearts, non-human primate cortex, and even in dorsal roots in humans[3–8].

Despite INS being used effectively in several applications, there is currently an incomplete picture of the underlying biophysical mechanism(s). It is well established that INS is strongly dependent on the spatial and temporal thermal gradients from laser irradiation[9]. However, it is unknown if other contributions have a significant role in the overall mechanism. Previous work from Shapiro *et al*. and Plaksin *et al*. showed a temperature-induced membrane capacitance increase specifically due to the phospholipid bilayer membrane thinning axially and expanding laterally[10,11]. However, a computational model developed by Peterson *et al*. indicated that capacitance is unlikely the sole mechanism because the capacitance change needed to generate an action potential is higher than what Shapiro *et al*. measured in lipid membranes[10,12]. Thermally activated Transient Receptor Potential Vanilloid (TRPV) channels have also been suggested as part of the mechanism. A TRPV blocker eliminated the action potential response from 1875 nm stimulation in retinal and vestibular ganglion cells, suggesting that TRPV channels are involved in the neural response of these neurons. Specifically, TRPV4 channels activated from heat led to an influx of calcium ions[13]. In cochlear stimulation, TRPV1 channels were shown to be important as most mice that lacked TRPV1 channels could not evoke action

potentials on the auditory nerve when stimulated optically[14]. By using capaszepine as a channel blocker in rat vagus nerves, TRPV1 was implied to be responsible for an increase in intracellular Ca^{2+} concentration[15]. Additionally, intracellular Ca^{2+} responses have shown to be induced by INS in *in vivo* rat somatosensory cortex[16], NG108 cells, CHO-K1 cells[17], neonatal cardiomyocytes[18], and *in vivo* mouse cortical neurons[19]. These studies have made significant progress toward uncovering the mechanism, but more work is still needed to fully understand how INS works biophysically.

Several studies have hypothesized that INS involves a photomechanical mechanism with shorter pulse widths. In a recent study by Throckmorton *et al*., different laser parameters of INS for rat sciatic nerve were compared. It was shown that a diode laser with a pulse width of 350 µs was not significantly different from a diode laser with a pulse width of 2 ms (Figure 2.1(a)). More interestingly, a Ho:YAG laser had a lower stimulation threshold than a diode laser with the same pulse duration of 350 µs and similar absorption coefficient (Figure 2.1(b)). Taking a closer look into the pulse structure of the lasers, the Ho:YAG laser has a large ~1 µs spike at the beginning of the pulse containing roughly 10% of the laser energy[20]. Removing the spike from the Ho:YAG pulse resulted in a higher stimulation threshold than the native Ho:YAG pulse, indicating the spike is likely responsible for the superior stimulation efficacy. When looking at stress vs. thermal confinement zones[21], a 1 µs pulse is much closer to stress confinement (calculated $\tau_{str} = \delta/\sigma =$ 220 ns for $\lambda = 2120$ nm) than the longer 350 µs pulse duration, supporting the idea of a mechanical component being the driving force behind the lower stimulation threshold. Furthermore, Shapiro *et al*. showed that pulses shorter than 2 ms evoked inward currents shorter in duration and higher in amplitude than 10 ms pulses[10]. Following the same trend, the stimulation threshold for rat brain slice cultures decreased with pulse width using photoabsorber-induced neurothermal stimulation[22]. Overall, stimulation appears to be more effective with shorter pulses, which potentially contain a mechanical component as these pulses are closer to stress confinement.

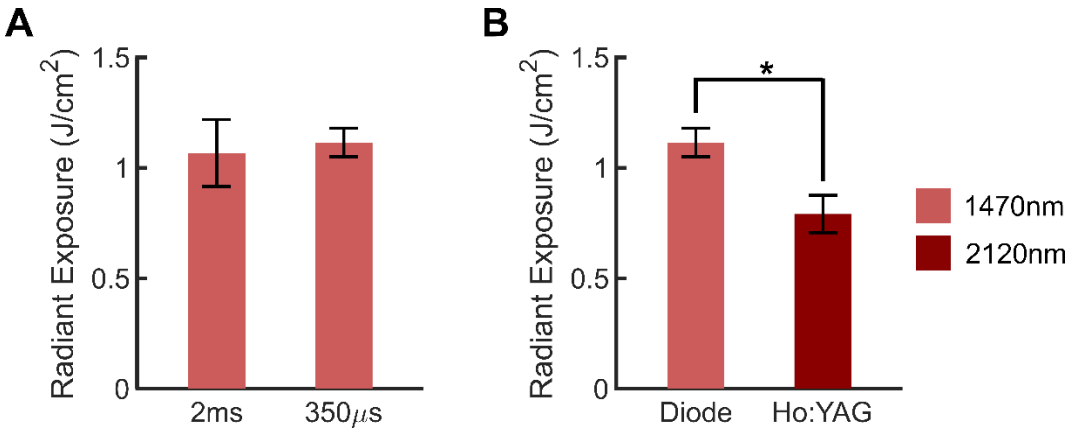

Figure 2.1 Stimulation thresholds across different laser parameters. (a) Pulse width does not significantly change the stimulation threshold of a diode laser at 2 ms and 350 µs (b) A Ho:YAG laser has a lower stimulation threshold than a diode laser despite having the same pulse width of 350 µs. Figure from Throckmorton *et al.*[20] licensed under CC BY 4.0.

A photomechanical mechanism has also been implicated in cochlear INS. Both direct neural stimulation and stimulation via an acoustic event have been discussed as possible mechanisms in the cochlea. Laser-induced pressure waves in water have been recorded from pulsed 1850 nm light, which indicated that laser-evoked acoustic events could cause stimulation in the cochlea[23,24]. More evidence of an optoacoustic pressure wave from the laser light acting on the basilar membrane as the main mechanism of cochlear stimulation was found from *in vivo* experiments on hearing guinea pigs with pressure measurements[25]. Additionally, in gerbil cochlea, Izzo *et al*. demonstrated that the stimulation thresholds for pulses up to 100 µs increased slightly, and the threshold was significantly higher for a 300 µs pulse[26], suggesting a mechanical contribution for the shorter pulses. However, there has also been data that show that an acoustic event does not dominate stimulation but rather direct radiation of neural tissue[27], making it unclear what the mechanism truly is.

Laser-induced stress and volumetric thermal expansion have previously been considered as the mechanism, but the conclusions from the experimental results dismissed a photomechanical contribution to the mechanism[9]. Since then, supporting evidence of a mechanical component to the mechanism has been more apparent with different stimulation

thresholds at shorter pulses and a possible mechanical mechanism in cochlear stimulation. Based on these findings and the fact that shorter pulses are closer to stress confinement than longer pulses, we hypothesize that a mechanical component is involved in shorter pulses that results in more efficient stimulation. Using computational modeling, we can obtain an understanding of the underlying biophysics during an infrared pulse on an incident nerve. This thesis aims to investigate possible mechanical effects in peripheral nerve INS by comparing transient pressure waves and displacement modeling results to experimental stimulation thresholds at different pulse widths.

2.2 Methods

2.2.1 SESE Model

The Scalable Effects Simulation Environment (SESE) is a software package developed by Nanohmics (Austin, TX) in collaboration with the Airforce Research Laboratory (AFRL) at Fort Sam Houston in San Antonio, TX that simulates physical effects of electromagnetic radiation impinging on a complex inhomogeneous structure. SESE version 2.6.0 was used for all simulations. Time-dependent simulations in 3D were run with set geometries for the neuron's structure, laser parameters, and material properties as inputs. The details of SESE's implementation can be found in a publicly released technical report[28] and are briefly described here.

The optical component of the model is implemented using Monte Carlo, a statistical method to determine the spatial distribution of radiation in an object. SESE's radiative transport is performed using probabilistically weighted traced rays from the source which undergo reflection and refraction when interacting with boundaries. Within the material, absorption and scattering occur probabilistically according to the material's optical properties.

For the thermal model, a Gauss-Seidel red-black successive over-relaxation (RBSOR) method[29] is used to solve the heat equation in the 3D domain with a finite volume discretization. The RBSOR technique allows for rapid convergence, eliminates the need to store large matrices, and is easily parallelized. The bioheat equation for the temperature T [K] over time t is:

$$\rho c \frac{\partial T}{\partial t} = \nabla \cdot (\kappa \nabla T) + \omega p_b c_b (T_b - T) + Q$$

where ρ is density [kg/m^3], c is specific heat [J/kg·K], κ is thermal conductivity [W/m·K], ω is the perfusion coefficient [1/s], and ρ_b, c_b, and T_b are the density [kg/m^3], specific heat [J/kg·K], and temperature [K], respectively, of the perfusive medium. Q is the source term [W/m^3], which is the radiative energy distribution from the optical model. Radiative, convective, evaporative, and ablative boundary conditions can be selected and applied to the object's surface.

The latest addition to SESE includes a numerical implementation of thermally mediated photoacoustic effects. In short, linear elastic equations with a thermal expansion term are solved with an elastic finite-difference time-domain solver. The elastic modulus λ [Pa], shear modulus μ [Pa], and thermal expansion coefficient α [1/K] are the material-dependent mechanical properties needed to solve for the transient pressure response. The elastic and shear moduli are Lame's parameters and can be calculated given the Young's modulus E [Pa] and Poisson ratio ν:

$$\lambda = \frac{E\nu}{(1+\nu)(1-2\nu)}$$

$$\mu = \frac{E}{2(1+\nu)}$$

2.2.2 Modeling parameters

For modeling peripheral nerve INS, the parameters and geometry are based on the setup that was used by Throckmorton *et al*[20]. The geometry (Figure 2.2) is set up as a 1.5 mm diameter rat sciatic nerve embedded in a 4 mm x 4 mm x 2 mm block of tissue surrounded by air. Since the nerve is exposed to air, a free convective boundary was selected. The tissue material properties mimic skin and should not affect the simulation significantly as the nerve absorbs all the radiative energy. A 400 μm diameter optical fiber (NA=0.22) is placed 862 μm above the top surface of the center of the nerve with the fiber in air as the surrounding medium. The measured spot size at the tissue surface was ~ 500 μm (knife edge and confirmed with a Thorlabs beam profiler)[20], so this was used for the simulation radiant exposures.

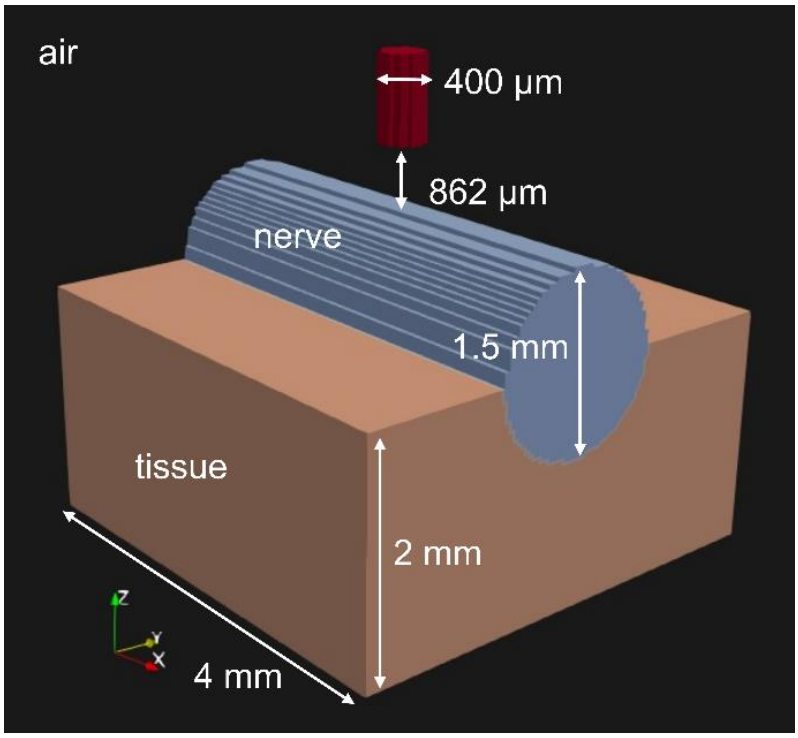

Figure 2.2 Geometry used for INS parameter simulations

Table 2.1 lists the optical, thermal, and mechanical properties used to model the mechanical response during INS on a rat sciatic nerve and polyacrylamide gel for model validation. The properties listed are assumed to be at an ambient temperature of 20°C, except for the volumetric thermal expansion coefficient which has temperature-dependent values.

Optical properties	**Material**	**Value**	**Reference**
Absorption Coefficient μ_a	Nerve	22.9 cm^{-1} at 1470 nm 22.7 cm^{-1} at 2120 nm	Ezekiel Haugen's work submitted for publication
	Water/gel	24 cm^{-1} at 2120 nm	[20,30]
Scattering Coefficient μ_s	Nerve	205.3 cm^{-1} at 1470 nm 173.5 cm^{-1} at 2120 nm	Ezekiel Haugen's work submitted for publication

	Water/gel	0 cm^{-1}	--
Anisotropy g	Nerve	0.9 at 1470 nm and 2120 nm	Ezekiel Haugen's work submitted for publication
Index of refraction	Water/nerve/gel	1.33	--
Thermal properties	**Material**	**Value**	**Reference**
Density ρ	Water/nerve	1075 kg/m^3	[31]
	Polyacrylamide gel	1030 kg/m^3	[32]
Thermal conductivity k	Water/nerve	0.49 W/m·K	[31]
	Gel	0.55 W/ m·K	[32]
Specific heat capacity c_p	Water/nerve	3613 J/kg·K	[31]
	Gel	3950 J/kg·K	[32]
Convection coefficient h	Ambient air	10 $W/m^2·K$	[33]
	Gel	N/A	--
Mechanical properties	**Material**	**Value**	**Reference**
Young's modulus E	Nerve	580,000 Pa	[34]
	Gel	25,000 Pa	[35]
Poisson ratio ν	Nerve	0.37	[36]
	Gel	0.474	[35]
Volumetric thermal expansion coefficient α_v	Water	0.0002°K^{-1} at 20°C 0.00025°K^{-1} at 25°C 0.0003°K^{-1} at 30°C	[37,38]

Table 2.1 Material properties

The optical, thermal, and mechanical properties of materials, especially live tissues, are difficult to measure. The properties listed here either use properties that were measured but might be in different experimental conditions or assume that of water since both nerve and polyacrylamide gel are mostly made up of water, which is the main chromophore for INS. Rat sciatic nerve optical properties have recently been collected from *ex vivo* fresh hydrated nerve by Haugen *et al*. (submitted for publication). Thermal properties of nerve are unknown and therefore are assumed to be that of water. The Young's modulus for nerve was taken from a fresh, whole rat sciatic nerve[34] and the Poisson ratio from fresh adult cadaver sciatic nerve[36]. For 10% polyacrylamide gel, the optical properties of water are assumed, and thermal properties were found in the literature. The volumetric thermal expansion coefficient of both nerve and gel is assumed to be that of water[37,38]. The gel thermal properties are based on a 10% concentration of acrylamide and 90% water[32]. The convection coefficient is set as 10 $W/m^2 \cdot K$, which is typical of free air convection[33].

2.2.3 SESE Model Validation

To confirm that the SESE model outputs are accurate, validation of the model is needed. The optical and thermal components of the model have been verified against analytical solutions, with more details in the technical report[28]. Additionally, skin damage thresholds from SESE photothermal modeling[39] compared well to experimental data[40]. The mechanical part has been compared to two existing models for verification, a published photoacoustic k-space propagation model[41] and COMSOL's linear elastic finite-difference time-domain code. Although SESE compares favorably to both these models, it has not been compared to experimental data and is therefore completed in this study.

2.2.3.1 SESE Displacement Validation

A previous study by Wells *et al*. measured the surface displacement of a rat sciatic nerve using differential phase optical coherence tomography (DP-OCT)[9]. To validate the displacement from the modeling results, the modeling inputs were set to match the Wells experimental setup. The geometry was configured for INS modeling on rat sciatic nerve using the geometry

mentioned above, with a Ho:YAG laser at a wavelength of 2120nm coupled to a 600µm diameter multimode fiber (NA = 0.39) placed 0.75mm from the surface of the nerve. The z-displacements were recorded from the model at radiant exposures 0.2, 0.4, 0.6, and 0.8 J/cm^2.

2.2.3.2 SESE Pressure Validation

For validating pressure from the SESE model, polyacrylamide gel was chosen as this gel is mostly made up of water but also has mechanical rigidity and similar mechanical properties to tissue. A 10% polyacrylamide gel was made with 0.1% bisacrylamide as the crosslinker and poured into a 5 cm x 5 cm x 5 cm 3D printed mold, which was mounted and has an opening that allows the optical fiber to be inserted into the gel from the bottom of the mold. A needle hydrophone (HNC-0200, ONDA, Sunnyvale, CA) was positioned 1mm away from the optical fiber using a micromanipulator. The laser and oscilloscope were triggered with a digital delay/pulse generator (DG535 Stanford Research, Sunnyvale, CA). Pressure waveforms were collected with PicoScope 7 software. A 350 µs pulse from the Ho:YAG coupled with a 600 µm fiber outputting 31mJ was tested. This pulse energy was used to stay below the ablation threshold. The modeling parameters were set up to closely match the experimental parameters used for validation. The parameters listed in the next section were used for investigating INS mechanical effects and are different from the validation parameters in this section.

2.2.4 Infrared neural stimulation parameters

Four different pulse duration and laser combinations (Table 2.2) were assessed for modeled pressures and displacements. Three of these laser parameters are taken from Throckmorton *et al*.: a free-running 350µs pulse from a 2120nm Ho:YAG laser, a 350µs pulse from a 1470nm diode laser, and a 2ms pulse from a 1470nm diode laser[20]. To investigate the effect of just the spike portion of the Ho:YAG pulse, this modeling study includes the addition of a short pulse Q-switched 2120nm Ho:YAG laser with a pulse duration of 100ns.

Laser	Wavelength (nm)	Nerve absorption coefficient (cm^{-1})	Pulse width (µs)	Spot size (µm)	Radiant exposures (J/cm^2)
Diode	1470	22.9	350	500	0.5 to 2
			2000		0.5 to 2
Ho:YAG	2120	22.7	0.1		0.5 to 2
			350		0.5 to 2

Table 2.2 INS Parameters

To be consistent with Throckmorton *et al*., a 400µm optical fiber (NA=0.22) was used for all INS simulations, and a 862 µm fiber-to-nerve distance was held constant. To assess the mechanical effects, specifically displacement and pressure, simulations were run for four different radiant exposures spaced evenly between 0.5 and 2 J/cm^2 for each laser parameter combination. To capture the pulse and effects after the pulse, simulations were run for a total of 1 ms for the 100 ns and 350 µs pulses and 4 ms for the 2 ms pulses.

2.2.5 Data analysis

The outputs from the model included temperature, displacement in x, y, and z directions, and the stress tensor at all positions in time and were visualized in ParaView. A single location at the surface of the nerve in the center was selected for observing the results where the laser pulse energy gets absorbed. Pressure is the negative of hydrostatic stress. From the stress tensor, we can calculate the pressure P as the average of the normal stresses:

$$P = -\frac{1}{3}\left(\sigma_{xx} + \sigma_{yy} + \sigma_{zz}\right)$$

2.3 Results

2.3.1 SESE displacement validation

Modeled z-displacements at the top surface of the nerve across radiant exposures 0.2-0.8 J/cm^2 (Figure 2.3(b)) are very similar to (within 5% of) DP-OCT displacements recorded by Wells *et al*. (Figure 2.3(a)). At 0.4 J/cm^2, the peak z-displacement is 295 nm, which is nearly the same displacement of 300 nm that Wells measured. The displacement over time at 0.4 J/cm^2 was only modeled up to 25 ms due to the heavy computation time but showed the same trend as the optical path length change of a rapid displacement change of ~300 nm and slow relaxation back to baseline.

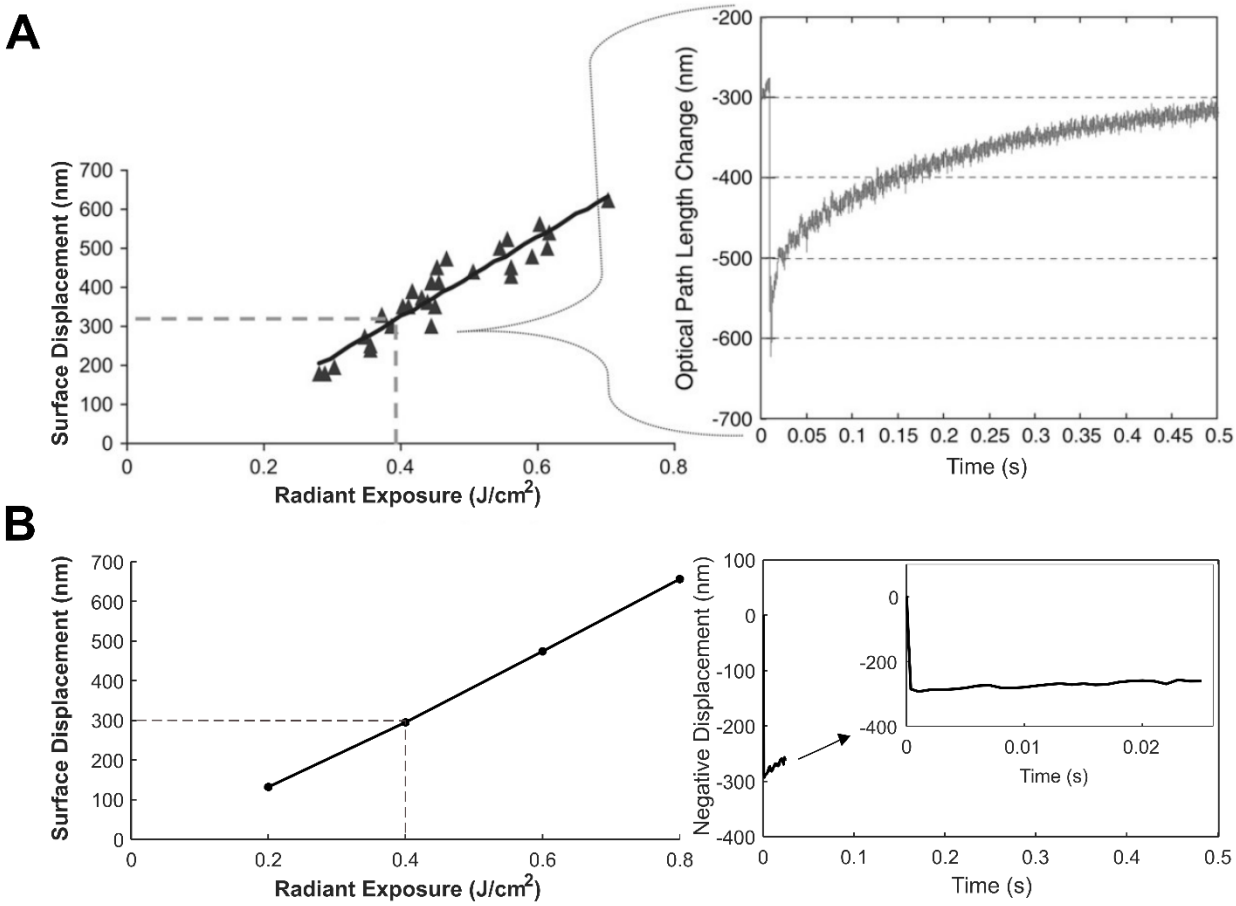

Figure 2.3 SESE model shows good agreement with experimental surface displacement values. (a) DP-OCT experimental results reproduced from Wells *et al*.[9] with permission from Elsevier. (Left) Surface displacement measurements over range of radiant exposures (Right) Optical path length change recording over time at 0.4 J/cm^2 corresponding to 300nm displacement (b) SESE model displacement results (Left) modeling displacements at 0.2 J/cm^2, 0.4 J/cm^2, 0.6 J/cm^2, and 0.8 J/cm^2. (Right) Modeled displacement over time at 0.4 J/cm^2 corresponding to 295nm displacement.

2.3.2 SESE pressure validation

The experimental setup for pressure validation is shown in Figure 2.4(a). For the pressure validation laser parameters (350 µs Ho:YAG pulse), both the experimentally measured and modeled pressures (Figure 4(b)) are very small (<100 Pa) and have positive (compressive) and negative (tensile) components. The experimental pressure is notably larger in magnitude than the modeled pressure, but both are on the same order of magnitude and oscillate similarly.

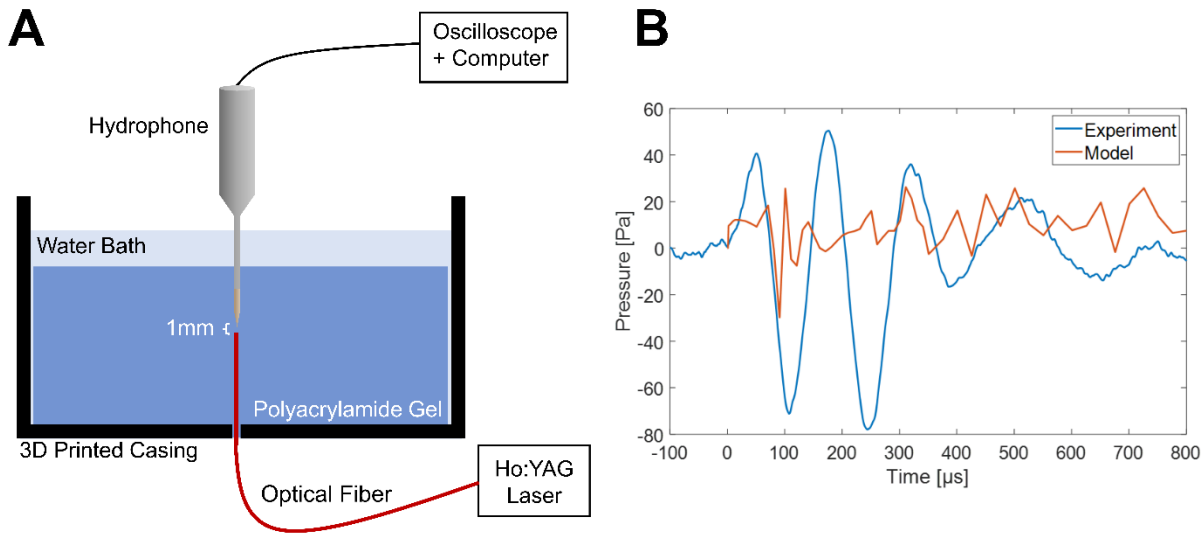

Figure 2.4 Pressure validation of SESE model. (a) Experimental setup for pressure validation of SESE model. The hydrophone was placed into 10% polyacrylamide gel 1 mm away from the 600 µm optical fiber. (b) Modeled vs. experimental pressure from free-running 350 µs Ho:YAG with 31 mJ output.

2.3.3 Temperature profiles

The modeled temperature rises across the different pulse durations and profiles are similar, with $\Delta T = 6.5°C$ for both Ho:YAG pulses (100 ns and 350 μs), 6.7°C for the diode 350 μs pulse, and 6.6°C for the diode 2 ms pulse (Figure 2.5(a-h)). Looking at the surface temperature over time (Figure 2.5(i)), each parameter shows the same trend: the temperature increases to the max temperature during the pulse, then diffuses slowly as time continues. As expected, the shorter pulses have a faster time to max temperature (dT/dt) since the pulse energy is deposited more quickly.

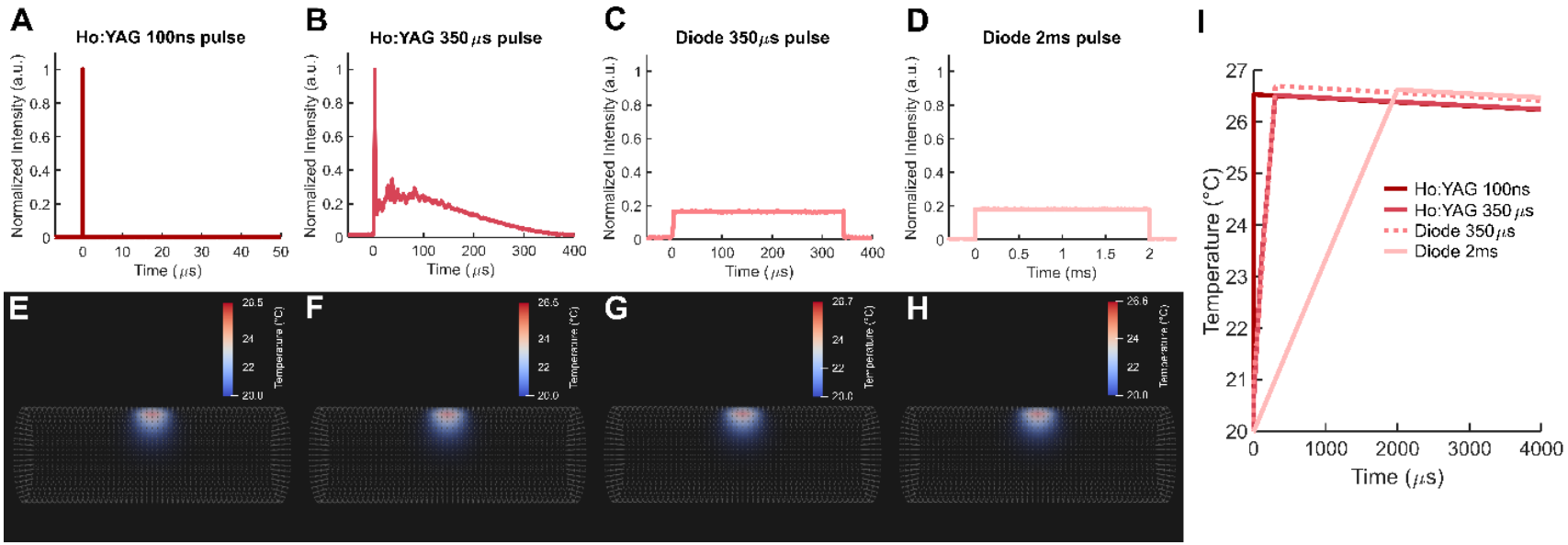

Figure 2.5 Temperature profiles across laser pulse profiles are similar. Area under curve-normalized temporal pulse profiles for (a) a 100 ns Ho:YAG pulse (b) free-running 350 µs Ho:YAG pulse (c) 350 µs diode pulse (d) 2 ms diode pulse. Spatial temperature profiles (1 J/cm^2) at the end of the pulse for (e) 100 ns Ho:YAG pulse, (f) free-running 350 µs Ho:YAG pulse, (g) 350 µs diode pulse, (h) 2 ms diode pulse. (i) Surface temperature over time compared across different parameters at 1 J/cm^2.

2.3.4 Displacement and pressure compared to stimulation efficiency

The displacement and pressure were modeled for a range of radiant exposures, showing a linear trend with radiant exposure. The maximum z-displacements across radiant exposures (Figure 2.6(a)) show that the100 ns Ho:YAG has slightly larger displacements than the other pulses, especially at higher radiant exposures. The other pulses have nearly identical max displacements. Similarly, the maximum pressure, defined as the maximum positive or compressive pressure, is identical across the pulses except for the 100 ns Ho:YAG, which has much higher pressures (Figure 2.6(b)). The minimum pressure, defined as the maximum negative or tensile pressure, is much larger in magnitude for the 100 ns pulse than the other pulses. Additionally, the 350 µs Ho:YAG pulse shows slightly larger negative pressure than the diode pulses (Figure 2.5(c)).

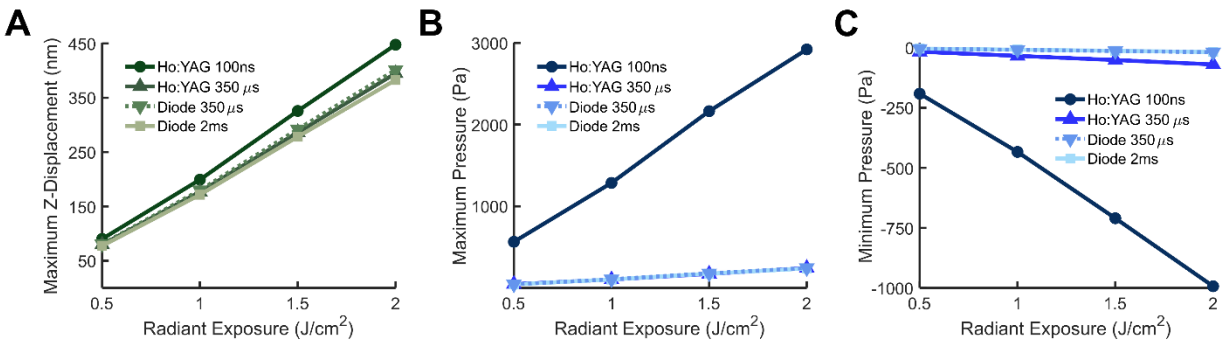

Figure 2.6 Maximum displacement and pressure are higher for shorter pulses across radiant exposures. (a) Maximum surface z-displacement (b) Maximum pressure, defined as the maximum positive or compressive pressure (c) Minimum pressure, defined as the maximum negative or tensile pressure, at the surface across a 100 ns Ho:YAG pulse, 350 µs Ho:YAG pulse, 350 µs diode pulse, and 2 ms diode pulse.

To draw a fair comparison, the displacement and pressure over time at the same radiant energy (1 J/cm^2) were examined. The x, y, and z-displacements over time are plotted for each pulse in Figure 2.7(a-d). The z-displacement is much higher than the x and y displacement. Each of the pulses reach similar max displacements, but the 100 ns Ho:YAG pulse has a higher z-

displacement and significant fluctuations. Minor fluctuations are also shown in the 350 µs pulses, more so in the Ho:YAG pulse than the diode. The pressure across the different pulses varied based on the pulse shape and duration (Figure 2.7(e)). A pressure spike with a much larger pressure (~1300 Pa) than any of the other pulses is evident for the 100ns Ho:YAG. There is also a spike for the 350µs Ho:YAG, but this is much smaller in magnitude (~100 Pa). For the overall duration of the pulse, the 350µs Ho:YAG and 350µs diode pulses have a similar rise in pressure to about 100 Pa. The 2ms pulse shows a very gradual linear pressure increase for the duration of the pulse. The stimulation thresholds previously determined by Throckmorton *et al*. are shown for comparison to the modeled mechanical effects (Figure 2.7(f)).

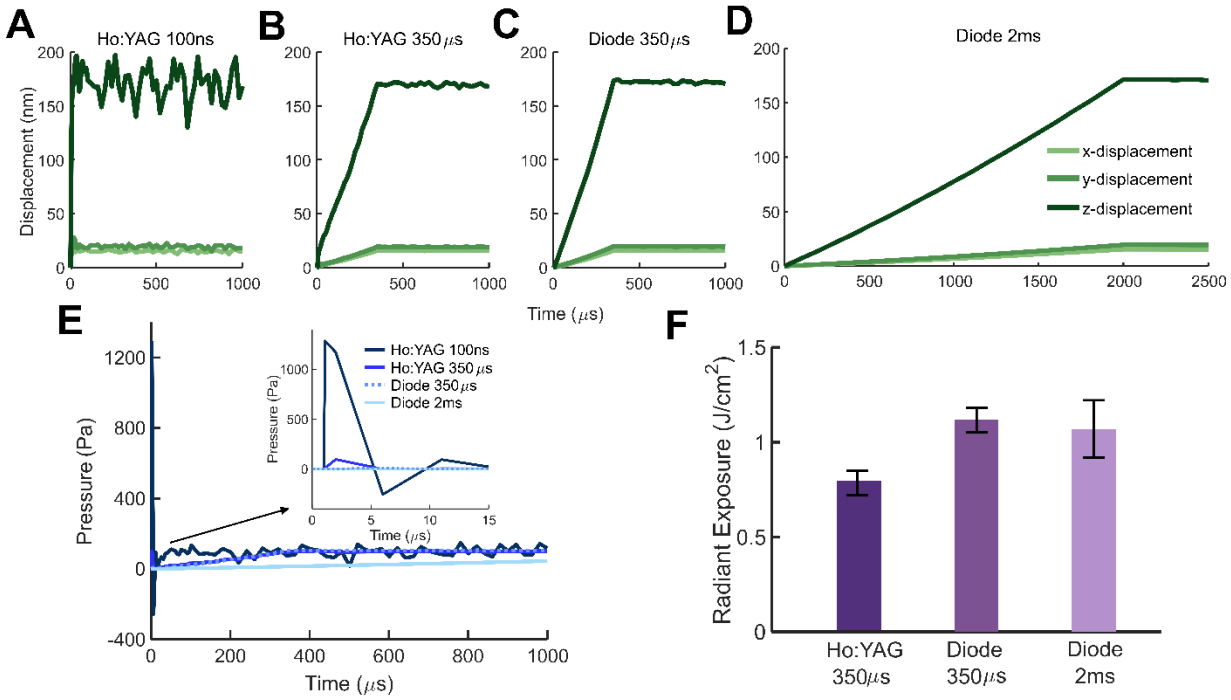

Figure 2.7 Displacement and pressure (1 J/cm^2) compared to stimulation threshold. (a-d) x, y, and z-displacement over time for 100 ns Ho:YAG pulse, 350 µs Ho:YAG pulse, 350 µs diode pulse, and a 2 ms diode pulse. (e) Pressure over time at 1 J/cm^2 (f) Stimulation thresholds for 350 µs Ho:YAG pulse, 350 µs diode pulse, and a 2 ms diode pulse. Adapted from Throckmorton *et al*.[20]

2.4 Discussion

Modeling the biophysical effects of INS computationally provides a deeper look into what exactly occurs during stimulation with a laser pulse. Thermal modeling of INS has been performed previously[42,43], as well as the characterization of a thermal gradient as part of the INS mechanism[9]. Recent evidence has pointed towards a mechanical component, but this has yet to be investigated for peripheral nerve INS. SESE provides a combined optical-thermal-mechanical model that is used here to determine the underlying mechanical effects of various laser parameters. To be able to accurately evaluate the results from the SESE model, it must first be validated. Surface displacement values for a rat sciatic nerve were compared to Wells *et al*. experimental data from 2007 and showed good agreement across multiple radiant exposures (Figure 2.3). Additionally, pressure measurements in polyacrylamide gel confirm that the pressures produced from INS energies for typical pulse durations (hundreds of µs or longer) are very small (<100 Pa) (Figure 2.4), especially compared to pressures involved in photoacoustic imaging (on the order of 10 kPa) or ultrasound (on the order of 1 MPa)[44]. While the experimental and modeling pressures do not match exactly, they both are such small pressures within the same order of magnitude. These pressures are difficult to experimentally measure and are minimal, which the modeling confirms. Future work with a short pulse Ho:YAG with low energy, which would induce higher pressures that are easier to measure, should be completed to further validate the model. With SESE's previous temperature validation[39,40], these validation results of displacement and pressure show that SESE is a promising tool that can be utilized for multiphysics modeling of different processes.

Since the discovery of INS, the mechanism has been hypothesized to be primarily a photothermal effect driven by water absorption from a thermal gradient. The spatial and temporal temperature profiles were modeled and examined for the different pulse parameters (Figure 2.5). Approximately the same temperature rise ($\Delta T = 6.6 \pm 0.1°C$) was observed for each of the pulses, but the rise time to the maximum temperature corresponded with pulse width. The diode pulses have slightly higher temperature rises than that of the Ho:YAG pulses, which can be explained by the higher absorption coefficient at 1470 nm ($\mu_a = 22.9\ cm^{-1}$) compared to the absorption coefficient at 2120 nm ($\mu_a = 22.7\ cm^{-1}$). Due to the longer pulse duration, which likely allowed some diffusion, the diode 2ms pulse has a slightly lower ΔT than the 350 µs pulse.

Following the rise to the maximum temperature at the end of the laser pulse, the temperature decays back to the baseline temperature over a thermal relaxation time τ_{th} which is defined as the time required for the peak temperature to decay to 1/e (37%) of the total temperature rise[45]. The thermal relaxation time is independent of pulse duration, and the calculated value (from $\tau_{th} = \delta/4\alpha$) is 215 ms while it was experimentally found to be 90 ms for rat peripheral nerve[9]. Although the 350 µs Ho:YAG and 350 µs diode pulses have nearly identical thermal gradients, the Ho:YAG has a lower stimulation threshold, which is hypothesized to be from the microsecond energy spike at the beginning of the pulse[20]. While the mechanism might be primarily photothermal, this difference in thresholds suggest other mechanisms might also be involved. Thompson *et al*. presented thermal modeling results that were compared to Izzo *et al*. and Richter et al. cochlea data[26,46,47] and suggested two regimes for stimulation: for pulses <100 µs, a minimum temperature is needed for stimulation and for pulses ≥100 µs, a thermal gradient is needed to achieve stimulation[42]. With the shorter pulses only needing a minimum temperature, some other contribution must be involved to achieve the stimulation the other pulses obtain with a thermal gradient. Together, these findings affirm the idea that multiple biophysical processes are involved in the INS mechanism.

Volumetric expansion occurs when a material expands due to heating, whereas thermoelastic expansion requires stress confinement (typically from a short pulse) and generates pressure waves. As shown in Figure 2.5, the different pulse parameters reach the same temperature over each respective pulse duration. Thus, the nerve would be expected to expand the same amount in each case. The modeled z-displacements represent the expansion of the nerve in the direction of the laser. Looking at the maximum displacement values (Figure 2.6(a)), all pulses had around the same surface displacement at each radiant exposure (~170 nm peak), but the 100ns pulse had a slightly higher displacement (~200 nm peak). When comparing the displacement over time at the same energy across the pulses (Figure 2.7 (a-d)), there are noticeably large fluctuations for the 100 ns pulse, smaller fluctuations for the 350 µs pulses, and no visible fluctuations for the 2ms pulse. These fluctuations can be attributed to vibrations occurring at the surface membrane, which likely causes membrane deformations. Plaskin *et al*. showed that a thermally induced deformation in the membrane induces a capacitance increase that leads to depolarization[11]. The displacement modeling results support the idea that volumetric expansion causes membrane deformations, which then induces a capacitance change. However,

this is likely not entirely a thermal effect. While the temperature gradient is quicker for shorter pulses which could lead to a larger capacitance increase, there seem to be underlying pressures from thermoelastic expansion that might also contribute, shown by the membrane fluctuations of the shorter pulses (100ns Ho:YAG and 350μs Ho:YAG with spike).

The modeling results show that pulse profiles impact transient pressures. Similar to how temperature-sensitive channels might be involved in the INS mechanism, we hypothesize that mechanosensitive channels could also play a role. Various mechanosensitive channels have been investigated for ultrasound stimulation. Yoo *et al*. found that in cortical neurons, mechanosensitive channels TRPP1/2, TRPC1, and Piezo1 respond to mechanical interactions, which then opens TRPM4 channels and causes depolarization[48]. TRAAK K^+ channels in *Xenopus* oocytes were found to be sensitive to pressure (-15 mmHg = -2000 Pa), which caused channel opening due to membrane tension [49]. Piezo2 was observed to be essential for mechanical firing in a subset of mouse sensory neurons[50]. Kubanek *et al*. showed that focused ultrasound modulates K^+ and Na^+ currents through K2P and $Na_v1.5$ channels[51]. The modeled pressures for INS parameters (100-1000 Pa at 1 J/cm^2) are very small, especially compared to those used for ultrasound neurostimulation (in the MPa range)[52]. However, a large pressure might not be needed to cause stimulation. In fact, Piezo2 was activated by a low threshold positive pressure (5 mmHg = 666 Pa)[53]. The small pressures found by these modeling results could be enough to activate mechanosensitive channels and help initiate stimulation.

Higher pressures resulted from shorter pulses (100 ns Ho:YAG) or pulses with a short energy spike (350 μs Ho:YAG). Our results also show that higher pressures correlate with lower stimulation thresholds, suggesting a mechanical effect leads to more efficient stimulation. Throckmorton *et al*. previously showed that a 350 μs Ho:YAG laser had a lower stimulation threshold than a 350 μs diode laser. These pulses have nearly identical temperature profiles at 1 J/cm^2 (Figure 2.5). Looking at the displacement and pressure, we can see the differences that the 1 μs spike of the 350 μs Ho:YAG causes, which includes a small pressure spike at the beginning and slightly more displacement fluctuations. The 350 μs and 2 ms diode pulses have similar stimulation thresholds but also have the same max pressure and displacement. The 100 ns pulse had a much higher pressure at 1 J/cm^2 in addition to a larger surface displacement with many fluctuations. We hypothesize that these more prevalent mechanical effects would lead to an even

lower stimulation threshold than that of the 350 µs Ho:YAG pulse. Further work should be done to determine the stimulation threshold of the short pulse Ho:YAG to confirm that mechanical effects are important in INS efficiency.

2.5 Conclusion

Computational modeling can be a useful tool for estimating the amplitude of photomechanical effects such as pressure transients during INS. There are higher magnitude mechanical effects, namely pressure and displacement changes, during shorter pulses or pulses with an initial energy spike. Higher magnitude pressure transients and larger displacement fluctuations also appear to correlate to lower stimulation thresholds. The data from this modeling study supports that shorter pulses result in more significant mechanical effects, specifically pressure and displacement changes, and thus supports the hypothesis that there is indeed a mechanical component to the INS mechanism. This insight will allow for finer tuning of the laser parameters needed for INS to move towards clinical applications.

2.6 References

1. Wells J, Kao C, Mariappan K, et al. Optical stimulation of neural tissue in vivo. *Opt Lett*. 2005;30(5):504. doi:10.1364/ol.30.000504

2. Wells J, Kao C, Jansen ED, Konrad P, Mahadevan-Jansen A. Application of infrared light for in vivo neural stimulation. *J Biomed Opt*. 2005;10(6):064003. doi:10.1117/1.2121772

3. Wells J, Konrad P, Kao C, Jansen ED, Mahadevan-Jansen A. Pulsed laser versus electrical energy for peripheral nerve stimulation. *J Neurosci Methods*. 2007;163(2):326-337. doi:10.1016/J.JNEUMETH.2007.03.016

4. Duke AR, Lu H, Jenkins MW, Chiel HJ, Jansen ED. Spatial and temporal variability in response to hybrid electro-optical stimulation. *J Neural Eng*. 2012;9(3):036003. doi:10.1088/1741-2560/9/3/036003

5. Izzo AD, Richter CP, Jansen ED, Walsh JT. Laser stimulation of the auditory nerve. *Lasers Surg Med*. 2006;38(8):745-753. doi:10.1002/LSM.20358

6. Jenkins MW, Duke AR, Gu S, et al. Optical pacing of the embryonic heart. *Nat Photonics 2010 49*. 2010;4(9):623-626. doi:10.1038/nphoton.2010.166

7. Cayce JM, Kao CC, Malphrus JD, Konrad PE, Mahadevan-Jansen A, Jansen ED. Infrared neural stimulation of thalamocortical brain slices. *IEEE J Sel Top Quantum Electron*. 2010;16(3):565-572. doi:10.1109/JSTQE.2009.2032424

8. Cayce JM, Wells JD, Malphrus JD, et al. Infrared neural stimulation of human spinal nerve roots in vivo. *https://doi.org/101117/1NPh21015007*. 2015;2(1):015007. doi:10.1117/1.NPH.2.1.015007

9. Wells J, Kao C, Konrad P, et al. Biophysical mechanisms of transient optical stimulation of peripheral nerve. *Biophys J*. 2007;93(7):2567-2580. doi:10.1529/biophysj.107.104786

10. Shapiro MG, Homma K, Villarreal S, Richter CP, Bezanilla F. Infrared light excites cells by changing their electrical capacitance. *Nat Commun*. 2012;3(1):1-11. doi:10.1038/ncomms1742

11. Plaksin M, Shapira E, Kimmel E, Shoham S. Thermal Transients Excite Neurons through Universal Intramembrane Mechanoelectrical Effects. *Phys Rev X*. 2018;8(1):011043. doi:10.1103/PhysRevX.8.011043

12. Peterson EJ, Tyler DJ. Activation using infrared light in a mammalian axon model. *Proc Annu Int Conf IEEE Eng Med Biol Soc EMBS*. Published online 2012:1896-1899. doi:10.1109/EMBC.2012.6346323

13. Albert ES, Bec JM, Desmadryl G, et al. TRPV4 channels mediate the infrared laser-evoked response in sensory neurons. *J Neurophysiol*. 2012;107(12):3227-3234. doi:10.1152/JN.00424.2011/ASSET/IMAGES/LARGE/Z9K0111213780007.JPEG

14. Suh E, Izzo Matic A, Otting M, et al. Optical stimulation in mice lacking the TRPV1 channel. In: *Https://Doi.Org/10.1117/12.816891*. Vol 7180. SPIE; 2009:112-116. doi:10.1117/12.816891

15. Rhee A, Li G, Wells J, et al. Photostimulation of sensory neurons of the rat vagus nerve. In: *Https://Doi.Org/10.1117/12.772037*. Vol 6854. SPIE; 2008:69-73. doi:10.1117/12.772037

16. Cayce JM, Friedman RM, Chen G, Jansen ED, Mahadevan-Jansen A, Roe AW. Infrared neural stimulation of primary visual cortex in non-human primates. *Neuroimage*. 2014;84:181-190. doi:10.1016/J.NEUROIMAGE.2013.08.040

17. Olsovsky CA, Tolstykh GP, Ibey BL, Beier HT. Origins of intracellular calcium mobilization evoked by infrared laser stimulation. In: *Https://Doi.Org/10.1117/12.2079895*. Vol 9321. SPIE; 2015:130-134. doi:10.1117/12.2079895

18. Dittami GM, Rajguru SM, Lasher RA, Hitchcock RW, Rabbitt RD. Intracellular calcium transients evoked by pulsed infrared radiation in neonatal cardiomyocytes. *J Physiol*. 2011;589(6):1295-1306. doi:10.1113/JPHYSIOL.2010.198804

19. Kaszas A, Szalay G, Slézia A, et al. Two-photon GCaMP6f imaging of infrared neural stimulation evoked calcium signals in mouse cortical neurons in vivo. *Sci Reports 2021 111*. 2021;11(1):1-18. doi:10.1038/s41598-021-89163-x

20. Throckmorton G, Cayce J, Ricks Z, Adams WR, Jansen ED, Mahadevan-Jansen A. Identifying optimal parameters for infrared neural stimulation in the peripheral nervous system. *Neurophotonics*. 2021;8(1):015012. doi:10.1117/1.NPH.8.1.015012

21. Jacques SL. Role of tissue optics and pulse duration on tissue effects during high-power laser irradiation. *Appl Opt Vol 32, Issue 13, pp 2447-2454*. 1993;32(13):2447-2454. doi:10.1364/AO.32.002447

22. Farah N, Zoubi A, Matar S, et al. Holographically patterned activation using photo-absorber induced neural–thermal stimulation. *J Neural Eng*. 2013;10(5):056004. doi:10.1088/1741-2560/10/5/056004

23. Teudt IU, Maier H, Richter CP, Kral A. Acoustic events and "optophonic" cochlear responses induced by pulsed near-infrared LASER. *IEEE Trans Biomed Eng*. 2011;58(6):1648-1655. doi:10.1109/TBME.2011.2108297

24. Schultz M, Baumhoff P, Maier H, et al. Nanosecond laser pulse stimulation of the inner ear—a wavelength study. *Biomed Opt Express*. 2012;3(12):3332. doi:10.1364/BOE.3.003332

25. Kallweit N, Baumhoff P, Krueger A, et al. Optoacoustic effect is responsible for laser-induced cochlear responses. *Sci Reports 2016 61*. 2016;6(1):1-10. doi:10.1038/srep28141

26. Izzo AD, Walsh JT, Ralph H, et al. Laser Stimulation of Auditory Neurons: Effect of Shorter Pulse Duration and Penetration Depth. *Biophys J*. 2008;94(8):3159-3166. doi:10.1529/BIOPHYSJ.107.117150

27. Young HK, Tan X, Xia N, Richter C-P. Target structures for cochlear infrared neural stimulation. *https://doi.org/101117/1NPh22025002*. 2015;2(2):025002. doi:10.1117/1.NPH.2.2.025002

28. Zollars BG, Early EA, Thomas RJ, Elpers GJ, Goodwin AL, Gamez NJ. Scalable Effects Simulation Environment (SESE) Version 2.5.0. Published online July 12, 2019. Accessed October 25, 2021. https://apps.dtic.mil/sti/citations/AD1082675

29. Zhang C, Lan H, Ye Y, Estrade BD. *Parallel SOR Iterative Algorithms and Performance Evaluation on a Linux Cluster*.; 2005. Accessed September 13, 2022.

https://apps.dtic.mil/sti/citations/ADA449212

30. Hale GM, Querry MR. Optical Constants of Water in the 200-nm to 200-μm Wavelength Region. *Appl Opt Vol 12, Issue 3, pp 555-563*. 1973;12(3):555-563. doi:10.1364/AO.12.000555

31. Hasgall P, Di Gennaro F, Baumgartner C, et al. IT'IS Database for thermal and electromagnetic parameters of biological tissues. Published online 2018. Accessed November 18, 2021. itis.swiss/database

32. Hirata Y, Kato Y, Andoh N, Fujiwara N, Ito R. Measurements of Thermophysical Properties of Polyacrylamide Gel Used for Electrophoresis. *J Chem Eng JAPAN*. 1993;26(2):143-147. doi:10.1252/JCEJ.26.143

33. Ng EYK, Ooi EH. FEM simulation of the eye structure with bioheat analysis. *Comput Methods Programs Biomed*. 2006;82(3):268-276. doi:10.1016/J.CMPB.2006.04.001

34. Borschel GH, Kia KF, Kuzon WM, Dennis RG. Mechanical properties of acellular peripheral nerve. *J Surg Res*. 2003;114(2):133-139. doi:10.1016/S0022-4804(03)00255-5

35. Boudou T, Ohayon J. An extended relationship for the characterization of Young's modulus and Poisson's ratio of tunable polyacrylamide gels. Published online 2006. Accessed August 17, 2022. https://www.researchgate.net/publication/6650233

36. Liu G, Zhang Q, Jin Y, Gao Z. Stress and strain analysis on the anastomosis site sutured with either epineurial or perineurial sutures after simulation of sciatic nerve injury. *Neural Regen Res*. 2012;7(29):2299. doi:10.3969/J.ISSN.1673-5374.2012.29.009

37. Xu S, Scherer GW, Mahadevan TS, Garofalini SH. Thermal Expansion of Confined Water. Published online 2009. doi:10.1021/la804061p

38. Popiel CO, Wojtkowiak J. Simple Formulas for Thermophysical Properties of Liquid Water for Heat Transfer Calculations (from 0°C to 150°C). *http://dx.doi.org/101080/01457639808939929*. 2007;19(3):87-101. doi:10.1080/01457639808939929

39. DeLisi MP, Gamez NJ, ClarkIII CD, Kumru SS, Rockwell BA, Thomas RJ.

Computational modeling and damage threshold prediction of continuous-wave and multiple-pulse porcine skin laser exposures at 1070 nm. *J Laser Appl*. 2021;33(2):022023. doi:10.2351/7.0000367

40. Delisi MP, Schmidt MS, Hoffman AF, et al. Thermal damage thresholds for multiple-pulse porcine skin laser exposures at 1070 nm. *https://doi.org/101117/1JBO253035001*. 2019;25(3):035001. doi:10.1117/1.JBO.25.3.035001

41. Cox BT, Kara S, Arridge SR, Beard PC. k-space propagation models for acoustically heterogeneous media: Application to biomedical photoacoustics. *J Acoust Soc Am*. 2007;121(6):3453. doi:10.1121/1.2717409

42. Thompson AC, Wade SA, Cadusch PJ, Brown WGA, Stoddart PR. Modeling of the temporal effects of heating during infrared neural stimulation. *J Biomed Opt*. 2013;18(3):035004. doi:10.1117/1.jbo.18.3.035004

43. Liljemalm R, Nyberg T, Von Holst H. Heating during infrared neural stimulation. *Lasers Surg Med*. 2013;45(7):469-481. doi:10.1002/LSM.22158

44. Beard P. Biomedical photoacoustic imaging. *Interface Focus*. 2011;1(4):602. doi:10.1098/RSFS.2011.0028

45. Choi B, Welch AJ. *Analysis of Thermal Relaxation During Laser Irradiation of Tissue*. Vol 29.; 2001.

46. Izzo AD, Walsh JT, Jansen ED, et al. Optical parameter variability in laser nerve stimulation: A study of pulse duration, repetition rate, and wavelength. *IEEE Trans Biomed Eng*. 2007;54(6):1108-1114. doi:10.1109/TBME.2007.892925

47. Richter CP, Bayon R, Izzo AD, et al. Optical stimulation of auditory neurons: Effects of acute and chronic deafening. *Hear Res*. 2008;242(1-2):42-51. doi:10.1016/J.HEARES.2008.01.011

48. Yoo S, Mittelstein DR, Hurt RC, Lacroix J, Shapiro MG. Focused ultrasound excites cortical neurons via mechanosensitive calcium accumulation and ion channel amplification. *Nat Commun 2022 131*. 2022;13(1):1-13. doi:10.1038/s41467-022-28040-1

49. Sorum B, Rietmeijer RA, Gopakumar K, Adesnik H, Brohawn SG. Ultrasound activates mechanosensitive TRAAK K+ channels through the lipid membrane. *Proc Natl Acad Sci U S A*. 2021;118(6):e2006980118. doi:10.1073/PNAS.2006980118/SUPPL_FILE/PNAS.2006980118.SAPP.PDF

50. Hoffman BU, Baba Y, Lee SA, Tong CK, Konofagou EE, Lumpkin EA. Focused ultrasound excites action potentials in mammalian peripheral neurons in part through the mechanically gated ion channel PIEZO2. *Proc Natl Acad Sci U S A*. 2022;119(21):e2115821119. doi:10.1073/PNAS.2115821119/SUPPL_FILE/PNAS.2115821119.SAPP.PDF

51. Kubanek J, Shi J, Marsh J, Chen D, Deng C, Cui J. Ultrasound modulates ion channel currents. *Sci Reports 2016 61*. 2016;6(1):1-14. doi:10.1038/srep24170

52. Blackmore J, Shrivastava S, Sallet J, Butler CR, Cleveland RO. Ultrasound Neuromodulation: A Review of Results, Mechanisms and Safety. *Ultrasound Med Biol*. 2019;45(7):1509-1536. doi:10.1016/J.ULTRASMEDBIO.2018.12.015

53. Shin KC, Park HJ, Kim JG, et al. The Piezo2 ion channel is mechanically activated by low-threshold positive pressure. *Sci Reports 2019 91*. 2019;9(1):1-9. doi:10.1038/s41598-019-42492-4